



Molten silicate interactions with thermal barrier coatings



Hengbei Zhao ^{a,*}, Carlos G. Levi ^b, Haydn N.G. Wadley ^a

^a Materials Science and Engineering, University of Virginia, Charlottesville, VA 22904, United States

^b Materials Department, University of California, Santa Barbara, CA 93106, United States

ARTICLE INFO

Article history:

Received 7 June 2013

Accepted in revised form 2 April 2014

Available online 12 April 2014

Keywords:

Thermal barrier coatings

Rare earth zirconate

CMAS reaction

ABSTRACT

The strain tolerance of thermal barrier coatings (TBCs) used in gas turbine engines is enhanced by incorporation of through-thickness pores within the coating. However, molten calcium–magnesium–alumino–silicate (CMAS) deposits are then able to permeate through the interconnected pore network resulting in dissolution of the coating in the silicate melt, precipitation of new phases, and the elimination of the pores needed for strain tolerance when silicate melt solidification occurs upon cooling. Here we used an electron beam directed vapor deposition method to deposit strain tolerant coatings containing a high volume fraction of inter-columnar pores to assess the effect of increasing the pore volume fraction upon silicate melt infiltration in a 7 wt.% yttria stabilized zirconia (7YSZ) TBC. We then explore two potential mitigation approaches. One investigated the infiltration of a samarium zirconate (SZO) coating deposited on a 7 wt.% yttria stabilized zirconia (7YSZ) buffer layer since recent work has indicated the related gadolinium zirconate (GZO) system was much more CMAS resistant than 7YSZ. The second explored the effects of an embedded platinum layer located near the outer surface of the SZO layer. The response of both systems to attack by a model 33CaO–9MgO–13AlO_{1.5}–45SiO₂ CMAS melt at 1250 °C has been compared to that of the 7YSZ composition coating deposited by the same process. The 7YSZ specimens were fully infiltrated by CMAS in less than 1 min and significantly dissolved and re-precipitated a globular phase after 4 h of exposure. The penetration rate in SZO coatings was reduced by about a factor of five, but the coatings were still completely penetrated after a 4 hour exposure. Significant SZO dissolution and precipitation of both globular fluorite and faceted apatite phases were observed after the 4 h of exposure, with concomitant debonding at the SZO/YSZ interface. The insertion of a 5 μm thick Pt layer about 30 μm below the SZO surface arrested permeation of CMAS for about 16 h and might provide a promising strategy for controlling CMAS degradation in TBCs without reducing the thermo-cyclic delamination resistance.

Published by Elsevier B.V.

1. Introduction

Thermal barrier coatings (TBCs) are widely used in the high pressure turbine section of gas turbine engines to reduce component temperatures and extend the life of internally cooled airfoils in the hot gas flow path [1]. Since the surfaces of components in future engines are likely to be cyclically exposed to temperatures of 1250 °C and above, Fig. 1 [47], the TBC must adhere well to these components, have a high delamination resistance and provide thermal protection [2,3]. In a typical TBC system, adherence under severe oxidizing thermo-cyclic loading conditions is achieved with an aluminum rich metallic bond coating that is applied to the airfoil. This is then thermally protected by a porous, low thermal conductivity ceramic topcoat; normally consisting of 6–8 wt.% yttria stabilized zirconia (7YSZ) [4]. Vapor deposited 7YSZ coatings have a columnar structure and contain a significant porosity. Some of the porosity is in the form of inter-columnar pores that can extend through the thickness of the coating [5]. These pores

result in a strain tolerant coating that can expand and contract during heating and cooling of the system, Fig. 2(a). Increasing the inter-growth column separation distance reduces the strain energy driving delamination, and increases the delamination resistance of thermal barrier coatings. Additional porosity is located on the surface of the growth columns and extends into their interior [6]. This “feathery” component of the porosity is highly effective at reducing the through thickness thermal conductivity of the coatings [7,8].

During high temperature operation of the coating system, an alumina rich, thermally grown oxide (TGO) layer gradually forms on the bond coat surface. As this layer grows in thickness over time, its large thermal expansion mismatch with other parts of the system results in a gradual build-up of internal strain energy upon cooling, and this eventually leads to coating delamination (spallation) [3,8]. The delamination resistance of TBC systems has been greatly improved by using bond coat alloy compositions that slow the rate of TGO thickening [2,9]. Additional improvements in delamination resistance have been achieved by reducing the elastic strain energy stored in the ceramic thermal insulation layer (by decreasing its in-plane elastic modulus through incorporation of inter-column and other pores) [2,7,8,10]. The inter-columnar gaps in

* Corresponding author. Tel.: +1 434 924 4084.
E-mail address: hengbei@virginia.edu (H. Zhao).

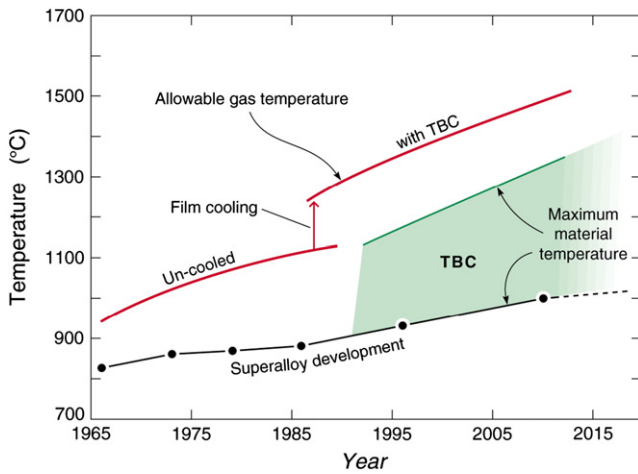


Fig. 1. The historical evolution of high pressure turbine gas temperature showing contribution of superalloy development, air cooling and thermal barrier coatings (TBCs). Adapted from a private communication from Robert Schafrik (2008).

coatings deposited using gas jet assisted processes can be increased by increasing the gas pressure [6], and coatings with high inter-column pore fractions have been shown to have significantly longer delamination lifetimes than those grown under normal high vacuum conditions [8]. Rare-earth (RE) zirconates ($\text{RE}_2\text{Zr}_2\text{O}_7$) have also attracted significant interest as a novel thermal protection layer because of their intrinsically lower thermal conductivities [11–14]. This enables the temperature at the bond coat surface to be further reduced, thus slowing the thermally activated TGO growth rate. The pyrochlore structure of many near equiatomic RE zirconates is also phase stable to higher temperatures than 7YSZ [15]. They also have a higher melting temperature than 7YSZ, and a greater resistance to morphological evolution of their pore structure (sintering) [13,16,17]. The combination of a high inter-column pore fraction and with a representative samarium zirconate (SZO) composition coating has resulted in coatings of very high through thickness thermal resistance and excellent delamination resistance [11,18].

Current gas turbines utilize only a modest fraction of the chemical energy available in the fuel–air system. Efforts to achieve more efficient fuel utilization have pushed increases in the engine operating temperatures, as indicated in Fig. 1. It is unfortunate that as the gas flow temperature rises in the high pressure turbine section of a gas turbine engine, ceramic thermal barrier coatings become increasingly vulnerable to attack by molten calcium magnesium alumino-silicate (CMAS) deposits resulting from the ingestion of siliceous particulates (dust, sand, volcanic ash, debris) with the intake of air [19–21]. Even when particle removal strategies are utilized, small diameter particles are still able to reach the turbine section, where they melt, wet the thermal protection coating surface, and then penetrate the coating by permeation through its interconnected network of inter-columnar pores, as schematically illustrated in Fig. 2(b) [19,22].

Thermal barrier coatings deposited by conventional electron beam vapor deposition processes contain a volume fraction of porosity, $\phi = 0.2$ distributed as inter-columnar gaps and the feathery pores on the sides of growth columns. As a result the initial permeability can be very high, and permeation of liquids of low viscosity can be rapid. As the surface temperature of a TBC increases, the viscosity of CMAS decreases rapidly and experimental studies indicate that CMAS penetrates deeply into thermal barrier coatings. For example, Krämer et al. found that molten CMAS at temperatures above 1240 °C can rapidly (and fully) penetrate the interconnected pores in a 100–200 μm thick 7YSZ coating [23]. The original 7YSZ then dissolves in the melt, and upon cooling precipitates a phase with globular morphology, and a composition that depends on the local chemistry. When the infiltrated and reacted layer solidifies upon engine cooling, the high modulus, large

thermal expansion coefficient and loss of strain tolerance (by filling of the inter-column pores) of this part of the coating lead to its delamination, Fig. 2(b) [24,25]. Coating processes such as directed vapor deposition (DVD), that utilize gas jets to increase the delamination resistance of the TBCs, can have much higher porosities with ϕ approaching 0.4 [26,27]. However, the effects of this higher porosity upon CMAS infiltration and coating degradation have not been investigated to date.

The effect of CMAS on a gadolinium zirconate ($\text{Gd}_2\text{Zr}_2\text{O}_7$, GZO) coating has also been recently studied [21]. It was found that GZO more effectively inhibited the penetration of CMAS than the 7YSZ system. Even after a 4 h exposure at 1300 °C, the CMAS melt had only infiltrated to a depth of $\sim 30 \mu\text{m}$. This was ascribed to rapid dissolution of the GZO and essentially concurrent precipitation of a stable crystalline apatite phase ($\text{Ca}_2\text{Gd}_8(\text{SiO}_4)_6\text{O}_2$) as well as fluorite and minor amounts of spinel from the GZO–CMAS melt. It has been proposed in the patent literature that this mitigation strategy can be implemented with the entire lanthanide series ($\text{RE} = \text{La} \rightarrow \text{Lu}$, as well as Y) [28,29], as long as the concentration of the dopant is sufficiently high (typically of order 50% $\text{REO}_{1.5}$). The $\text{A}^1\text{A}^{\text{II}}_6(\text{SiO}_4)_x$ apatite phase (hexagonal) has two cation sites, A^1 and A^{II} , with 9- and 7-fold coordination, respectively. It is reasonably well established that the A^{II} site is always occupied by the RE^{3+} with some minor incorporation of Zr^{4+} in apatites produced from CMAS reaction with RE zirconates [21]. However, the A^1 site can be occupied either (i) entirely by Ca^{2+} giving a stoichiometry $\text{Ca}_4\text{RE}_6(\text{SiO}_4)_6\text{O}_2$ with vacancies on the ionic O^{2-} sites, or (ii) entirely by the RE cation (and charge compensating cation vacancies) yielding $\text{RE}_{9.33}(\text{SiO}_4)_6\text{O}_2$ [30, 31] or (iii) a combination of Ca and RE as in $\text{Ca}_2\text{RE}_8(\text{SiO}_4)_6\text{O}_2$. It has been proposed that the first scenario applies to Y and the smaller lanthanides, e.g. Yb [32], with attendant benefits on the efficiency of the RE cation in capturing the primary components of the glass melt (SiO_2 and CaO) [28]. The rationale is that the smaller RE cations would not be compatible with the larger 9-fold coordinated sites, a hypothesis consistent with the observation that the Ca-free apatite $\text{RE}_{9.33}(\text{SiO}_4)_6\text{O}_2$ is observed primarily for the larger lanthanide cations ($\text{La} \rightarrow \text{Dy}$) [31, 33]. However, apatites with stoichiometry $\text{Ca}_2\text{Y}_8(\text{SiO}_4)_6\text{O}_2$ as well as $\text{Y}_{9.33}(\text{SiO}_4)_6\text{O}_2$ have been reported in the literature [34], at variance with the proposed stoichiometry for the smaller cations. Within this context, the present study explores the CMAS mitigation potential of the pyrochlore $\text{Sm}_2\text{Zr}_2\text{O}_7$ (SZO), a candidate TBC material sharing with GZO the attributes of lower thermal conductivity, enhanced phase stability and sintering resistance [17].

Recently Begley et al. have investigated the effects of thin plastically deformable metal layers embedded in ceramic coatings, upon TBC delamination during thermal cycling [10,18,35]. They identified combinations of constituent material properties (of the metal layer and ceramic coating) and relative proportions that reduced the delamination driving force considerably. For example in a Pt/YSZ system, 50% reductions of the elastic energy release rate could be achieved with a metal volume fraction of ~ 0.2 . Parallel experimental studies also led to the discovery that the presence of a Pt layer in the ceramic coatings significantly retarded the TGO growth rate, which contributed to a further increase in delamination life [36]. A final objective of the study is to therefore investigate if such an embedded platinum layer in a TBC coating could arrest the permeation of liquid CMAS into the coating.

The study described here first establishes a baseline response for the interaction of molten CMAS with a standard composition 7YSZ TBC coating made using a directed vapor deposition process that results in coatings with a higher ($2\times$) pore volume fraction than conventional EB-PVD coatings. It then explores the behavior of a highly porous samarium zirconate (SZO) coating deposited in the same way on a 7YSZ buffer layer. Finally the study investigates the response of a SZO/Pt/SZO coating, again deposited on 7YSZ. It is found that the highly porous 7YSZ and SZO coatings are both penetrated by CMAS. The apatite precipitation found in the GZO system is also present in SZO but is less effective in mitigating CMAS penetration in the latter than in GZO because of the higher porosity levels. In addition, significant coating

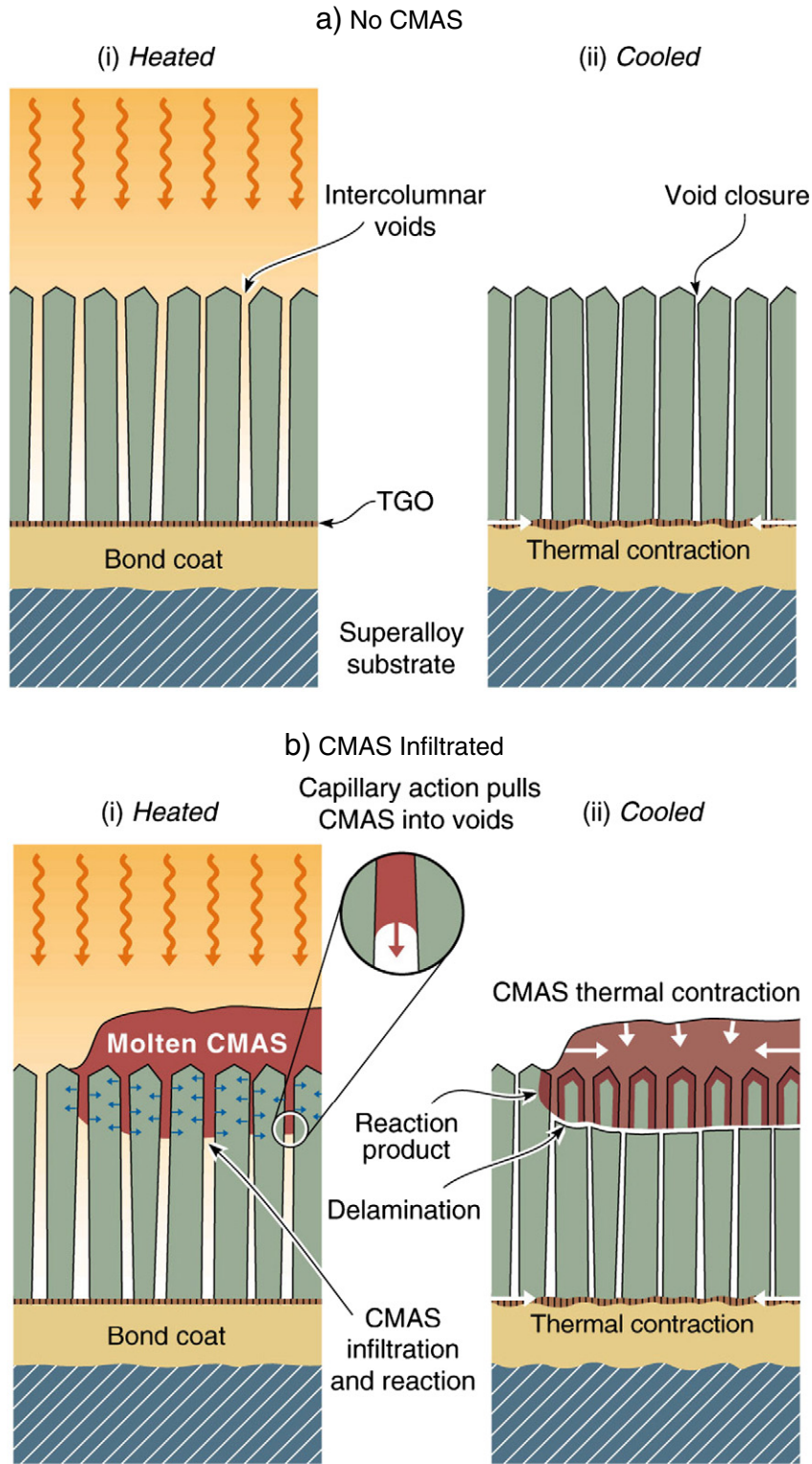


Fig. 2. (a) Normal operation of a thermal barrier coating system. Failure occurs near the TGO layer due to the large elastic strain energy stored in the TGO and TBC layers. The stored elastic strain energy is reduced in the TBC by use of wide inter-column gaps. (b) Molten CMAS penetration through a surface heated coating containing inter-column pores. Penetration stops when CMAS reaches regions that are below its melting point. On cooling the loss of the strain compliance in the TBC layer induces spallation of the infiltrated region.

dissolution is observed at the SZO–YSZ interface of the bilayer system when reached by the penetrating CMAS. This resulted in separation of the layers. We will show that a single 5–10 μm thick layer of Pt in a SZO coating is effective at limiting infiltration of CMAS for a 16 h exposure at 1250 $^{\circ}\text{C}$; providing a promising route for increasing both the delamination and the CMAS resistance of a coating.

2. Experimental procedures

Three types of coatings (7YSZ, SZO/7YSZ and SZO/Pt/SZO/7YSZ) were deposited on 99.5% purity, polycrystalline alumina substrates obtained from CoorsTek (Golden, CO), Fig. 3. Alumina substrates were used for the deposition because subsequent CMAS tests were conducted

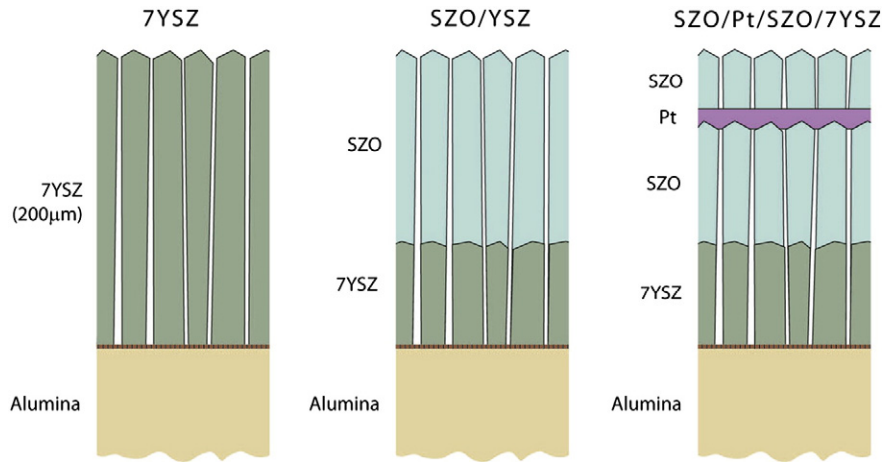


Fig. 3. Schematic illustration of the three coating types investigated in the study.

above 1200 °C and would have caused damage to conventional superalloy substrates. The $25 \times 25 \times 0.6$ mm substrates were coated using an electron beam directed vapor deposition technique [37,38]. In this approach a multi-source crucible was positioned in the throat of a supersonic helium gas jet forming nozzle, and each material was sequentially deposited on a substrate. A detailed description of the fabrication process and coating microstructures is presented elsewhere [11,18,36]. The 7YSZ and SZO ceramic source rods were 12.5 mm in diameter and were obtained from TCI Ceramics Inc. (Bethlehem, PA). The Pt rod was of the same diameter and obtained from ESPI Metals (Ashland, OR). The deposition temperature was 1000 °C and the substrates were rotated at the rate of 6 rpm during the deposition. This resulted in a deposition rate of about 3–5 $\mu\text{m}/\text{min}$. The coatings were all ~ 200 μm thick. The SZO/7YSZ bilayer coating had a 70 μm thick 7YSZ buffer layer on which the SZO was grown. The 5 μm thick Pt layer in

the SZO/Pt/SZO/7YSZ coating was placed about 30 μm from the outer surface of the SZO coating. Fig. 4 shows micrographs at low and high magnifications of the 7YSZ and SZO coatings used in the study. The coatings contained nominally straight inter-columnar pores (that were almost identical in length to the coating thickness) and feathery pores that extended from the surface to the center of all the growth columns. The total pore fractions of the 7YSZ and SZO coatings were both $\sim 40\%$, and were measured from the weight and volume change when coatings were deposited on the alumina substrates. In both coatings about $60 \pm 5\%$ of this porosity consisted of inter-columnar pores.

The “as fabricated” samples were subjected to a CMAS test protocol used in prior studies [23]. A model CMAS composition of $33\text{CaO}-9\text{MgO}-13\text{AlO}_{1.5}-45\text{SiO}_2$ (all in mole percent of single cation based oxide formulae) or $\text{C}_{33}\text{M}_9\text{A}_{13}\text{S}_{45}$ was adopted for this investigation. This composition began to melt at 1235 °C and was completely molten

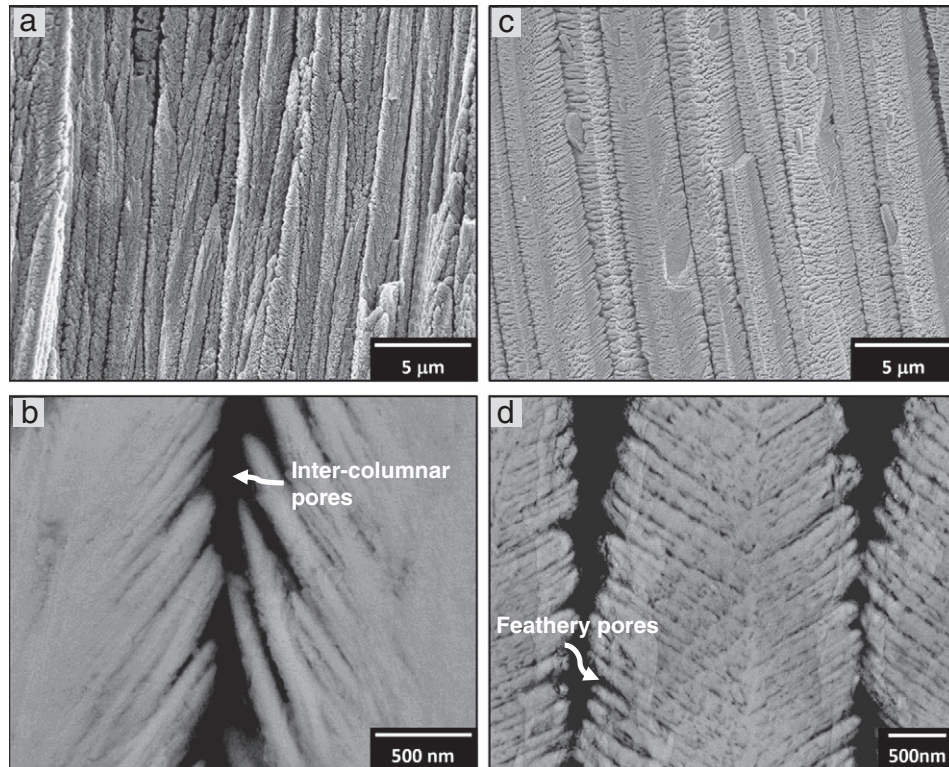


Fig. 4. The morphology of vapor deposited 7YSZ (a, b) and SZO (c, d) thermal barrier coatings showing many pores present within and between growth columns.

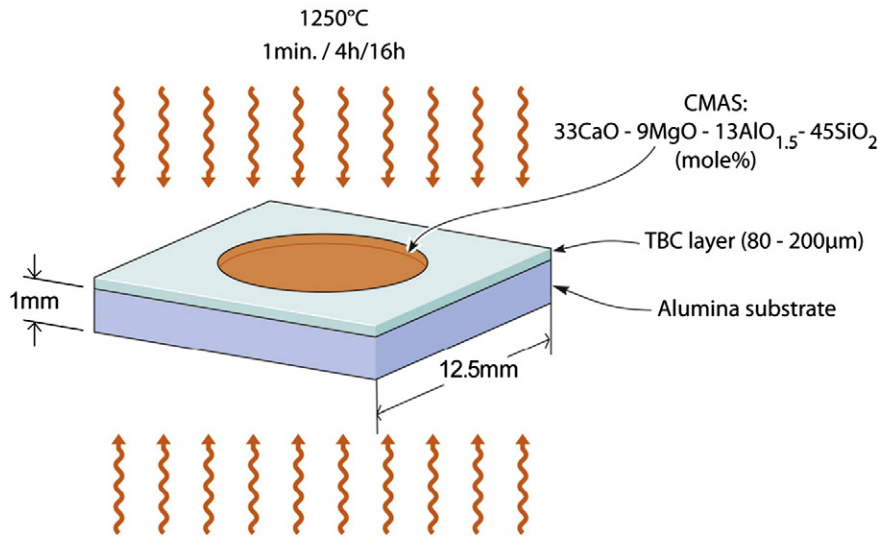


Fig. 5. Sample geometry and isothermal CMAS infiltration test methodology.

at 1240 °C. The CMAS was prepared by cold-pressing the pre-reacted powder into a 6 mm diameter pellet with a weight of ~45–50 mg. The pellet was then placed on the surface of TBC specimens, Fig. 5. The samples were heated in an air environment furnace to 1250 °C at a rate of 6 °C/min and held at this temperature for 1 min,¹ 4 h or 16 h followed by cooling at a rate of 6 °C/min.

The surface morphology of the CMAS infiltrated specimens was examined by scanning electron microscopy (SEM). Samples were then sectioned by cutting the specimen on a plane perpendicular to the axis of rotation during coating deposition. The specimens were mounted in epoxy and polished using a 0.5 μm diameter diamond suspension. Backscatter electron (BSE) images and the compositions of various phases were obtained using a scanning electron microscope (JOEL JSM 6700F) equipped with energy dispersive X-ray spectroscopy (EDS). Transmission electron microscopy (TEM) specimens were prepared by a “lift-out” technique using a FEI Helios 600 dual-beam FIB microscope. A 20 × 10 × 1.5 μm thick slice was prepared that included the reaction layer between the coating and CMAS. This was lifted out and placed on a copper grid. Further thinning of the sample was then performed with the sample on the grid (using a modest ion beam current to minimize FIB damage) until the specimen was electron transparent which corresponded to a final foil thickness of ~110 nm. The TEM samples were examined in a JEOL 2000FX 200 keV transmission electron microscope.

3. Results and interpretation

3.1. 7YSZ coatings

Cross-sectional images of the 7YSZ specimens after 1 min and 4 h of exposure to molten CMAS are shown in Fig. 6. The Ca:Zr and Y:Zr atomic concentration ratio profiles through the coating thickness are overlaid on each figure. The average Y:Zr ratio was 0.09, consistent with the nominal ratio of $7.6\text{YO}_{1.5}/92.4\text{ZrO}_2 = 0.082$. Composition measurements on the coating exposed to CMAS for 1 min, Fig. 6(a), indicate the presence of calcium, with an average Ca:Zr ratio of 0.1, throughout the coating. After a more prolonged exposure, Fig. 6(b), the calcium to zirconium fraction had increased to an average value of ~0.14. We note that the molar volume of CMAS and 7YSZ is estimated to have similar values of ~20.7 and 20.3 cm³/g-mole, respectively [21]. Since the coatings had a porosity of ~40%, and were fully filled with CMAS

(0.33CaO), the calculated atomic Ca:Zr ratio would be 0.24. The measured ratio of 0.14 (measured after a 4 h CMAS exposure) therefore indicates a volume fraction of 0.23 CMAS, implying that 58% of the initial pore volume was infiltrated after a 4 h exposure. For a Ca:Zr ratio of 0.1

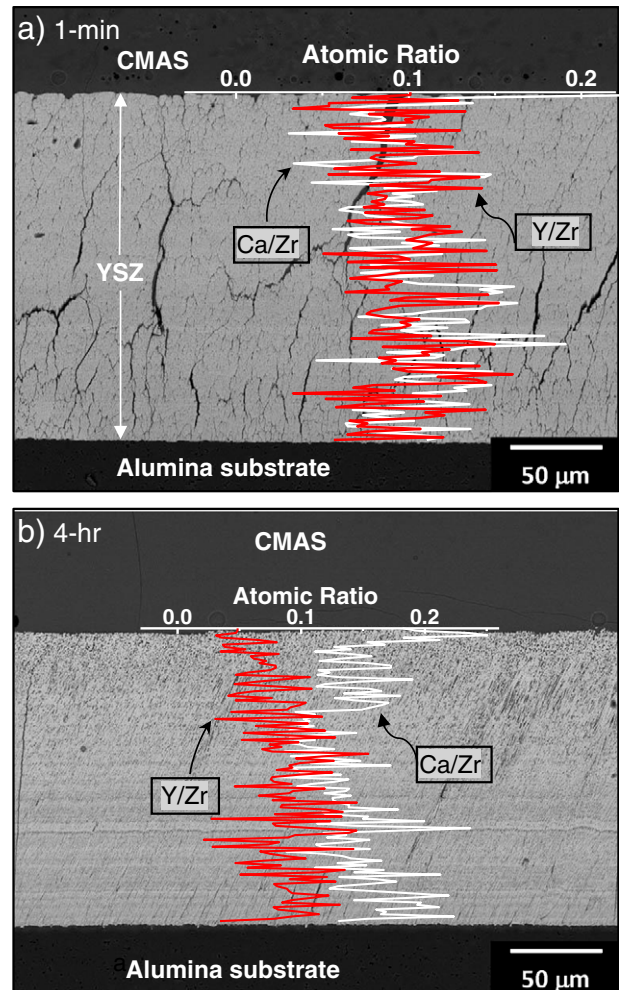


Fig. 6. Depth composition analysis for 7YSZ samples exposed to CMAS at 1250 °C for (a) 1 min and (b) 4 h.

¹ Note that melting starts ~15 °C below the hold temperature, so the 1 min hold actually represents about 5 min total where the TBC is in contact with silicate melt.

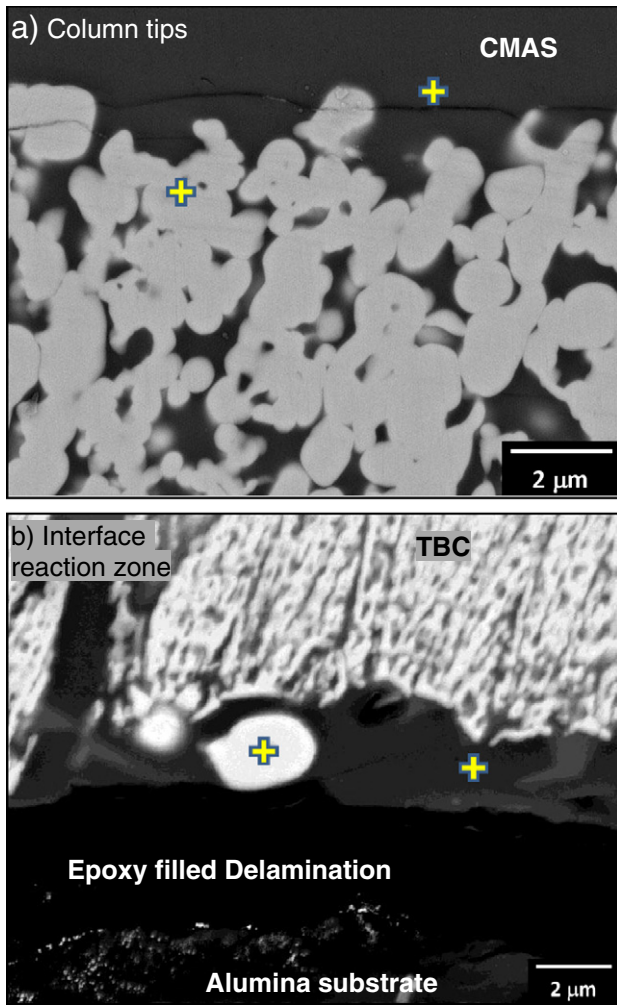


Fig. 7. (a) The outer surface column tips and (b) TBC/substrate interface in a YSZ TBC specimen exposed to CMAS at 1250 °C for 4 h. The crosses correspond to locations of composition measurements.

(measured after a 1 min exposure) the volume fraction of CMAS would be 0.165, and the pore volume fraction filled is 42% of the total. It can be therefore concluded that the molten CMAS rapidly permeated the 200 μm thick 7YSZ coating at 1250 °C, filling about ~40% of the pores after a minute of exposure and ~60% of the pores after a 4 h of exposure.

The reactions within the 7YSZ coating upon this CMAS infiltration have been further investigated. Fig. 7 shows high magnification views of the top and bottom surfaces of the 7YSZ coating after a 4 h CMAS exposure. In both locations significant reactions and morphological transformations had occurred. At the coatings' outer surface, Fig. 7(a), the column tips had lost their characteristic faceted pyramidal shapes. These were replaced by an agglomeration of globular particles that form an interconnected network interpenetrated by CMAS, Fig. 7(a), consistent with the observations of Krämer et al. [23]. EDS analysis of the region marked by a cross is given in Table 1 and reveals that the globular particles have a low $YO_{1.5}$ content of ~2.3 at.% rather than 7 at.% as in the original 7YSZ, and also incorporated some CaO (~1.6 at.%) presumably in solid solution. Their composition is consistent with the transformable tetragonal ZrO_2 phase identified [23]. Fig. 7(b) shows the structure at the bottom TBC–alumina substrate interface. Much of the interface had debonded upon cooling, and then filled with epoxy during sample preparation. Directly above this epoxy filled crack, a pore free (gray) phase with elongated morphology was identified. An EDS composition analysis for the region marked by the cross on the right is shown in Table 1, and indicates concentrations of Ca, Al and

Table 1
Chemical composition of regions in upper and lower reaction zones of 7YSZ.

Region	Ca	Mg	Al	Si	Y	Zr
CMAS near the column tips	35.9	5.4	11.9	44.5	0	2.3
Globular particles at the surface column (at.%)	1.6	0	0	0	2.3	96.1
Globular particles at the interface (at.%)	3.5	0	0	0	11.9	84.6
Elongated particles at the interface (at.%)	21.1	0	33.8	43.6	0	1.5

Si consistent with the stoichiometry of anorthite ($CaAl_2Si_2O_8$) whose presence has also been previously reported by Krämer et al. [23]. This layer also contained isolated large globular (white) particles. The globule marked by the cross on the left contained ~11.9 at.% $YO_{1.5}$ and ~3.5 at.% CaO, Table 1, consistent with the fluorite ZrO_2 phase reported elsewhere [23].

In summary, the compositional depth profile and EDS composition analysis of the various particles indicate that molten CMAS rapidly infiltrated the inter-columnar (through thickness) pores of the highly porous DVD 7YSZ coating and began to penetrate towards the roots of the feathery pores within the growth columns. About 60% of the pores were filled with CMAS after a 4 h, 1250 °C exposure. This is consistent with complete penetration of the inter-columnar pores and partial filling of the feathery component of the pore structure. The rate of CMAS penetration is consistent with that observed by Krämer et al. in conventionally deposited 7YSZ with a lower porosity. Concurrent with infiltration, the CMAS melt dissolved the YSZ columns, especially at

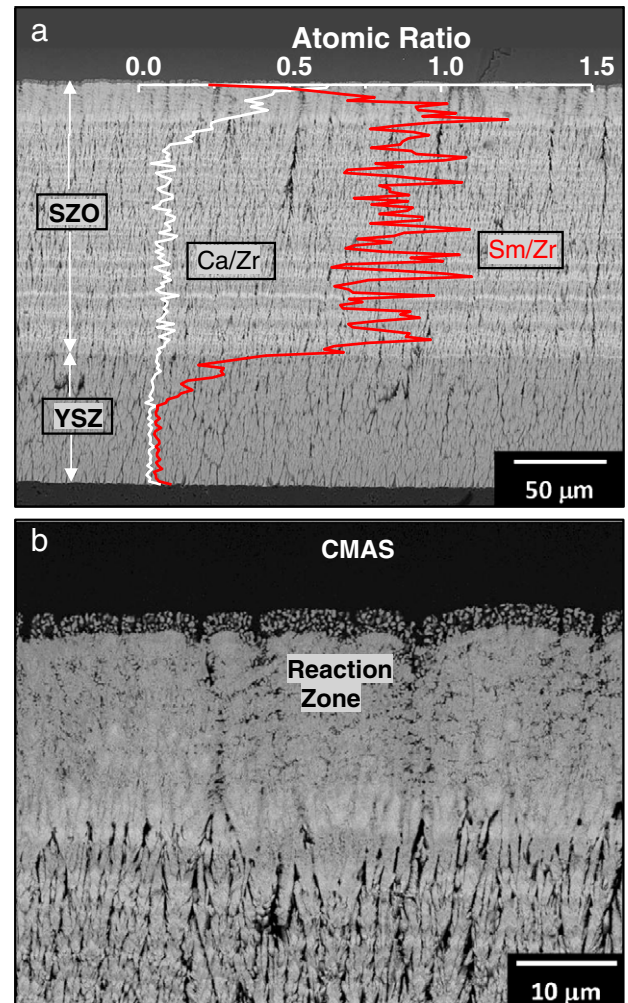


Fig. 8. Cross-sectional micrographs of SZO/YSZ bi-layer samples exposed to CMAS for 1 min: (a) the depth profile chemical analysis and (b) the reaction zone of the top columns.

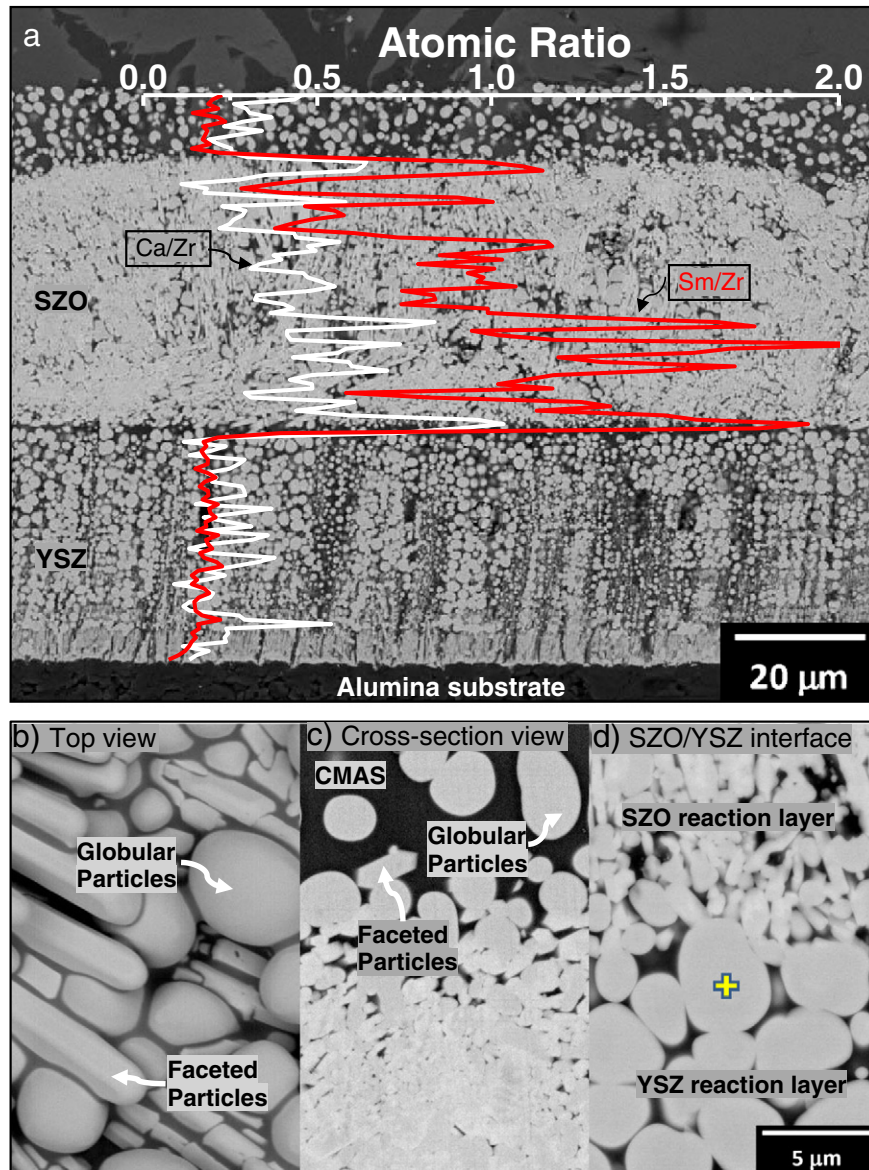


Fig. 9. (a) SZO/YSZ bi-layer samples exposed to CMAS at 1250 °C for 4 h with composition depth profiles, (b) top (plan) view of the SZO/YSZ bi-layer sample, (c) cross-sectional slice of the top reaction zone between CMAS and SZO, and (d) the interface between SZO and YSZ. Note that the black ground is the glassy CMAS material.

the tips and roots, and re-precipitated zirconia solid solutions with modified composition as well as silicate reaction products. EDS examination reveals that ~2.3 at.% Zr has been dissolved in the CMAS near the column tips. The globular solid solution phases were Y-lean near the surface and Y-enriched near the substrate. This is consistent with dissolution and diffusion of the surface yttrium into the CMAS reservoir above the coating, and in agreement with the observations by Krämer et al. Anorthite was formed by reaction of the alumina substrate with CMAS that penetrated to the YSZ–alumina interface. Upon cooling, delamination cracks at the YSZ and alumina substrate interface relieved the significant stored strain energy in the 7YSZ coating (e.g. Fig. 7b);

Table 2
EDS composition analysis for the top reaction zone in SZO.

Constituent	Ca	Mg	Al	Si	Sm	Zr
CMAS	31.0	6.6	10.5	47.7	1.2	3.0
Globular Particles (at.%)	4.7	0	0	0	6.4	88.9
Faceted Particles (at.%)	14.9	0	0.6	39.8	32.2	12.5

a consequence of its loss of compliance due to filling of the TBC's pore structure with solidified CMAS and melt-coating reaction products.

3.2. SZO on 7YSZ bilayer coatings

Fig. 8 shows the cross sections of an SZO/YSZ bilayer specimen (with a total SZO porosity of 40%) after exposure to CMAS for 1 min at 1250 °C. The banding structure can be seen in the coating, which resulted from the composition fluctuation during deposition. The significant vapor pressure difference of the constituent species (Sm_2O_3 and ZrO_2) has created melt instabilities leading to unsteady evaporation of the two species. This phenomenon has been described and explained elsewhere [11]. EDS line scans of the Ca:Zr and Sm:Zr atomic concentration ratios

Table 3
Chemical composition (at.%) for the SZO/YSZ interface reaction zone.

Region	Ca	Mg	Al	Si	Zr	Sm	Y
CMAS	28.0	6.1	18.7	40.1	4.4	2.6	0.1
Globular particles	4.5	0	0	0	88.0	5.8	1.7

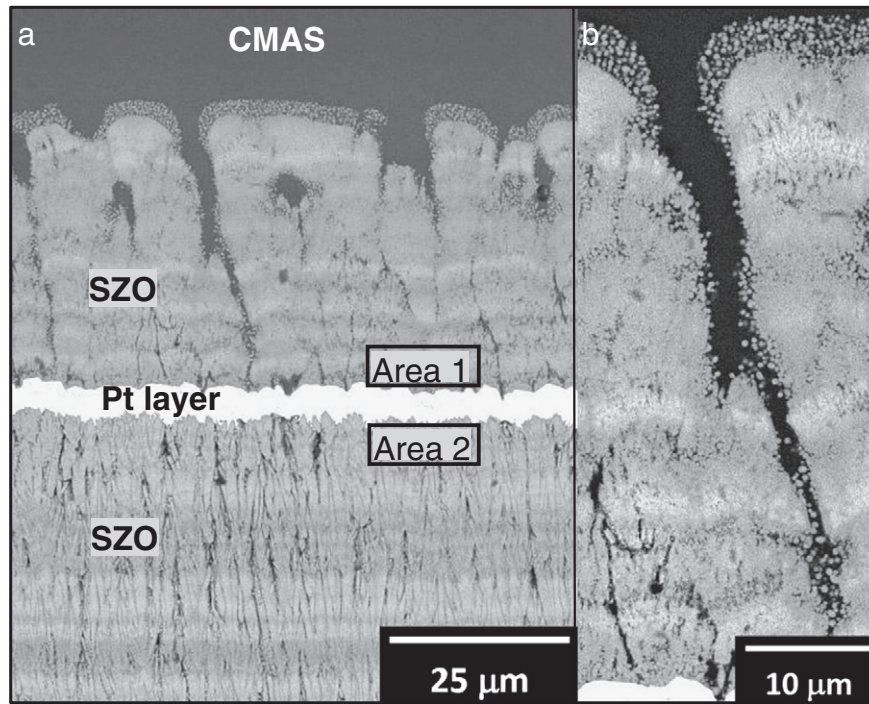


Fig. 10. SZO/Pt/SZO/YSZ coating after exposure to CMAS for 1 min. The inset (b) shows a higher magnification view of the upper SZO layer in contact with CMAS.

through the thickness of the coating are overlaid on the SEM micrograph in Fig. 8(a). It is evident that CMAS had penetrated the SZO layer to a depth of only ~30 μm following a 1 min liquid CMAS exposure. Calcium was not detected in significant amounts within the coating beneath this depth. A higher magnification image of the near surface region, Fig. 8(b), clearly shows that the column tips had reacted to form a network of small globular and needle-like faceted particles with the intervening space filled with CMAS. Just beneath the SZO surface some of the faceted particles had crossed the inter-columnar gaps, and this appears to have impeded (but not arrested) the inward flow of CMAS.

As the CMAS exposure time was increased to 4 h, Fig. 9(a), the CMAS fully penetrated both the SZO and YSZ layers of the bilayer coating. The interface between the SZO and YSZ layer had also separated while at 1250 °C, and had filled with (now solidified) CMAS. A Ca EDS line scan analysis, Fig. 9(a), confirms the presence of Ca throughout the coating. An extensive morphological reconfiguration, suggestive of dissolution and re-precipitation processes, was also evident at the top of the SZO coating where the concentration of CMAS was highest. Top and cross-sectional views of the surface reaction layers are shown in Fig. 9(b) and (c), respectively. The reaction layer contained faceted particles in addition to the globular particles reminiscent of those found in YSZ. These particles at the top of the coating, Fig. 9(b), were located in a region originally occupied by the tips of the growth columns and co-existed with a high volume fraction of CMAS.

Table 4
EDS analysis (at %) for area 1 (above) and area 2 (below) Pt layer.

Sample	Region	Ca	Mg	Al	Si	Sm	Zr	Pt
1-min exposure	Area 1	10.1	0.5	3.4	10.3	42.5	31.5	1.6
	Area 2	0.3	0	0	0	51.8	46.5	1.4
4-h exposure	Area 1	9.3	0.3	1.6	12.2	40.2	35.3	1.1
	Area 2	0.3	0	0	0.1	49.8	48.6	1.2
16-h exposure	Area 1	15.3	0.1	0	16.5	30.1	36.3	1.7
	Area 2	0.3	0	0	0.3	57.8	40.3	1.3

The compositions of the two particles and CMAS were investigated by EDS analysis, Table 2. The globular particles consisted primarily of oxides of Zr with smaller amount of Ca and Sm. This is consistent with a zirconia-based solid solution containing Sm and Ca. The EDS analysis also revealed that the faceted particles were a silicate phase similar to the apatite phase seen in GZO, but containing predominantly Sm, Zr, and Ca. The (Ca + Sm + Zr):Si ratio was approximately 60:40, or 9:6. Because Zr^{4+} would substitute on the A^II site, the inferred stoichiometry would be approximately $[Ca_{0.59}Sm_{0.28}□_{0.13}]_4[Sm_{0.67}Zr_{0.33}]_6(SiO_4)_6O_2$ suggesting that 13% of the A^I sites are vacant, a slightly higher proportion than that found in GZO, but consistent with the higher proportion of Zr^{4+} incorporated in the A^II sites [21]. In comparison, the fraction of vacant A^I sites in the Ca-free apatite $Sm_{9.33}(SiO_4)_6O_2$ would be ~17%. Moreover, Zr^{4+} incorporation can lead to enhancement in the Ca content due to charge compensating effects, as reflected in the higher Ca concentration reported in Table 2 (14.9%) relative to the nominal formulation, i.e. 12.5%.

Fig. 9(a) revealed that the original SZO columns, clearly evident after 1 min, were no longer identifiable after the 4 h exposure, and were replaced by a two-phase mixture of globular and faceted particles interpenetrated by residual CMAS. These two particle types completely occupied the original SZO coating volume. The chemical analysis suggests that the particles close to the SZO/YSZ interface had nearly the same composition as those near the surface implying that the nature of the reaction is essentially invariant of depth.

After a CMAS exposure of 4 h, the CMAS had reached and dissolved the 7YSZ buffer layer, and re-precipitated large globular YSZ particles, resulting in the physical separation of the SZO/YSZ interfaces as they were penetrated by CMAS, Figs. 9(a) and (d). An EDS analysis of the globular particles at the interface of SZO and YSZ, Table 3, was consistent with a zirconia phase containing Sm, Y and Ca. The particles have a very similar Ca and Sm composition to the particles in the upper surface reaction zone, but now also contained 1.7 at.% Y from the partially dissolved YSZ buffer layer and are shown below to be fluorite. The compositions of the CMAS on top and deep inside the coating in Tables 2 and 3 reveal that the $SmO_{1.5}$ and ZrO_2 fraction dissolved in the melt increased slightly between the top and interfacial regions, from 1.2 to

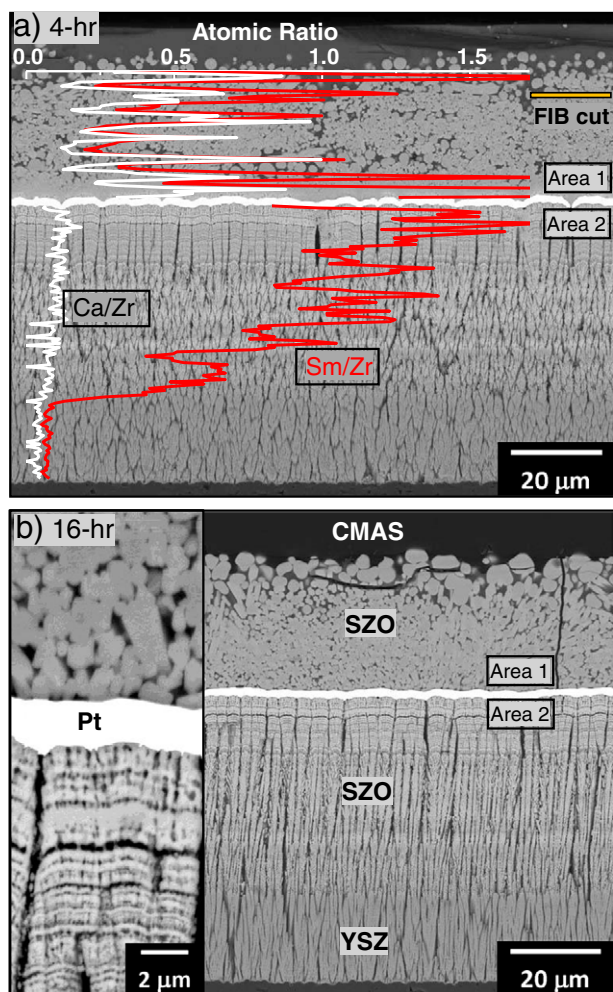


Fig. 11. (a) Depth profile chemical analysis for a SZO/Pt/SZO/YSZ coating exposed to CMAS at 1250 °C for 4 h. (b) A cross-sectional image of a similar sample exposed to CMAS attack at 1250 °C for 16 h.

2.6% for Sm^{3+} and 3.0 to 4.4% for Zr^{4+} , presumably because of changes in the local melt–crystal equilibria.

The composition analysis above indicates that the average Ca:Zr atomic ratio of the infiltrated coating was ~ 0.43 . The calculated molar volume of CMAS and SZO are ~ 20.7 and $22.2 \text{ cm}^3/\text{g-mole}$ respectively, and the SZO coating has a total pore fraction of $\sim 40\%$, so a fully infiltrated SZO coating would have a Ca:Zr ratio of 0.47. The measured average ratio of 0.43 after a 4 h exposure implies that $\sim 90\%$ of the porosity had been infiltrated.

3.3. SZO/Pt/SZO on 7YSZ

The effect of a short (1 min) molten CMAS exposure upon the SZO/Pt/SZO/YSZ coating can be seen in Fig. 10. The inter-columnar gaps in the top SZO layer again provided an efficient pathway for molten CMAS transport towards the Pt interface. The SZO column tips and sides above the $5 \mu\text{m}$ thick Pt layer had partially reacted with CMAS to form globular particles with CMAS present in the wide (several microns) inter-particle gaps, Fig. 10(b). To determine the effectiveness of the Pt layer in impeding molten CMAS transport, areas just above (Area 1) and beneath the Pt layer (Area 2) were chosen to do EDS analysis, Fig. 10(a). These results are presented in Table 4. In the area just above the Pt layer, the high Ca and Si concentrations indicate that CMAS had reached the upper surface of the Pt layer. However, the absence of these elements below the Pt layer

indicated that it was effective at impeding the transport of CMAS in the through thickness direction.²

The SZO/Pt/SZO/YSZ coatings were then exposed to CMAS for 4 and 16 h. Fig. 11 shows cross-sectional images of coatings CMAS-exposed for both times. In both cases, the SZO layer above the Pt layer had fully reacted with CMAS whereas below the Pt layer, there was almost no evidence of CMAS permeation. A compositional line scan analysis was performed on the specimen exposed to CMAS for 4 h and the Ca:Zr and Sm:Zr ratios are overlaid on the SEM micrograph shown in Fig. 11(a). No significant Ca or Si (and by inference no CMAS) was detected in the coating below the Pt layer indicating that the metal layer remained an effective barrier to CMAS infiltration. The inset in Fig. 11(b) shows a magnified view of reacted and non-reacted SZO layers separated by the Pt layer after a 16 hour exposure. The SZO coating below the Pt layer still maintained the columnar microstructure, and further confirms the view that this Pt layer retained its ability to arrest CMAS permeation. Table 4 shows the EDS determined compositions for areas identified as 1 and 2 above and below the Pt layer (locations shown in Fig. 11(a)) for CMAS exposures of 1 min, 4 and 16 h. The results are consistent with no significant CMAS penetration of the Pt layer. However, 1–2 at.% Pt was detected both in the CMAS zone (presumably due to dissolution by CMAS) and below the Pt layer within the SZO layer indicating that significant Pt transport had occurred within the TBC coating.

Careful examination of the coatings exposed to CMAS at 1250 °C for 1 min, 4 h and 16 h shows that the Pt layer gradually decreased in thickness (from 5 to $3 \mu\text{m}$) as the exposure time was increased to 16 h, presumably due to slow dissolution in CMAS and transport within the coating. In one area of the sample exposed to CMAS for 16 h, the Pt layer had begun to agglomerate, creating several small holes in the Pt layer, Fig. 12. It was noted that the as-deposited platinum layers did contain regions that were locally thinner; the thinnest of these may have failed first, allowing CMAS to then slowly penetrate into the coating through the small holes. The depth of penetration is outlined in blue in Fig. 12(a).

To identify the structure of the globular and faceted phases in the SZO–CMAS reaction zones, TEM samples were extracted by FIB in the location identified in the upper right of Fig. 11(a). A bright field TEM image is shown in Fig. 13(a). Both the globular and faceted (needle-like) particle types can be seen in a CMAS matrix. The electron diffraction patterns for the faceted particles, Fig. 13(b) and (c), indicate that their structure has a hexagonal symmetry with lattice constants $a = 9.8 \text{ \AA}$ and $c = 6.6 \text{ \AA}$. An EDS analysis of this phase, Table 2, is consistent with a silicate containing Sm, Zr and Ca, such as the apatite-type phase observed in the related GZO system, but with $a = 9.5 \text{ \AA}$ and $c = 6.9 \text{ \AA}$ [21].

4. Discussion

Examination of the infiltrated microstructures indicates that molten CMAS wets both YSZ and SZO surfaces, and rapidly penetrates into the inter-columnar gaps and eventually the feathery pore structure on the sides of the growth columns, consistent with the observations of Krämer et al. [23]. The problem can be modeled as a first approximation by infiltration of a liquid into a porous bed, wherein the velocity, v , at which a silicate melt flows through a porous body of thickness L is given by Darcy's law [39]:

$$v = \frac{\kappa}{\mu} \left(\frac{\Delta p}{L} \right) \quad (1)$$

where κ is the permeability of the porous body, μ the viscosity of the fluid and Δp the pressure drop driving the flow. While this expression

² A very small Ca signal was detected during the composition analysis. However, it was within the measurement error of the equipment and consistent with observations of coatings not exposed to CMAS.

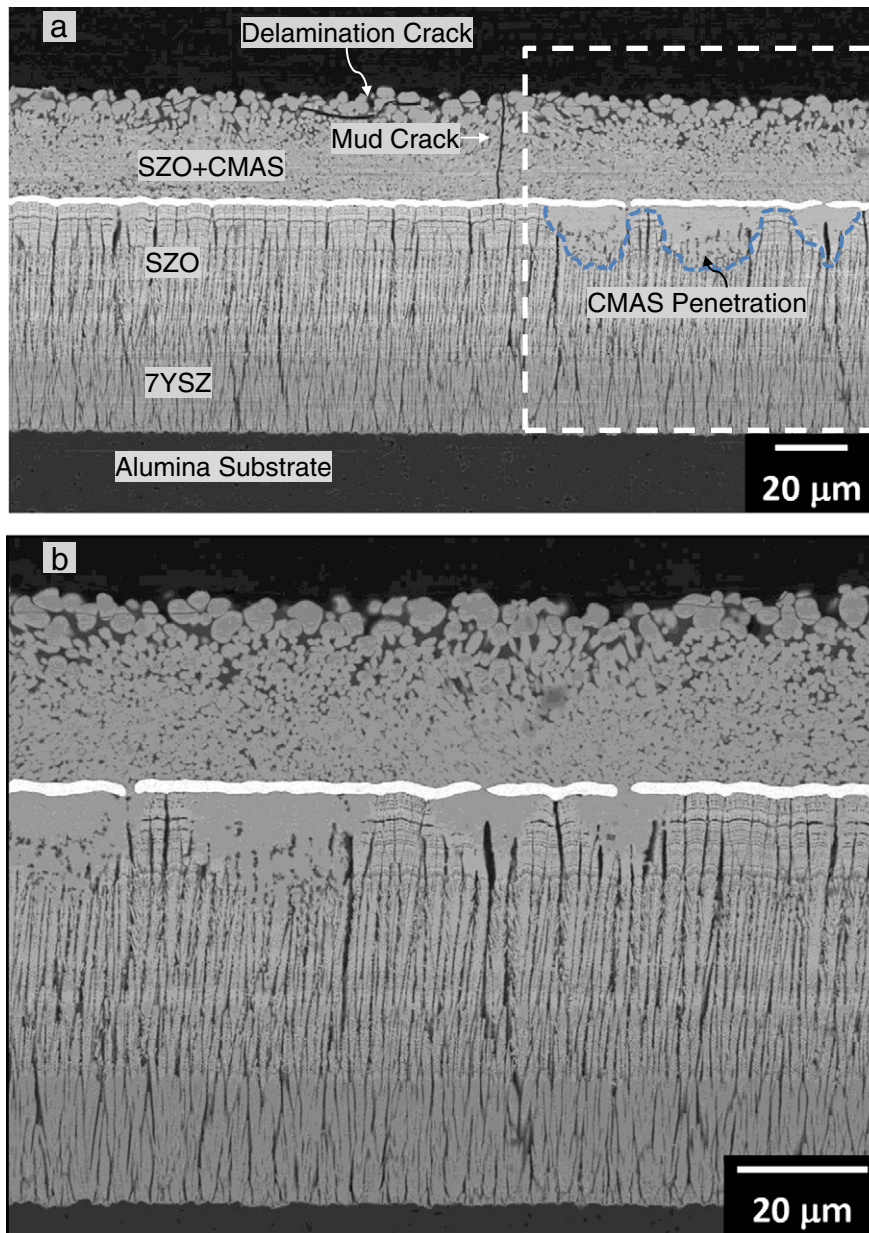


Fig. 12. Isolated pinholes in the Pt layer of a SZO/Pt/SZO/YSZ coating exposed to CMAS for 16 h at 1250 °C. In (a), the region of CMAS penetration below the Pt layer is outlined blue. The white dotted area is shown at higher magnification in (b).

is for steady state flow, it is assumed for the purposes of the present discussion that one can approximate the dynamic situation of an infiltration front in the same manner, with $v = dL / dt$ where L is the infiltrated thickness. The approach is further related to the physical characteristics of the medium by assuming that the porous body consists of an array of tortuous cylindrical capillaries of radius r , with the permeability given by the Carman–Kozeny model:

$$\kappa \approx \frac{r^2}{8\tau^2} \phi \tag{2}$$

where ϕ is the pore fraction and τ is a pore tortuosity factor that may be assumed of order unity for intercolumnar pores that are relatively straight paths from the surface into the TBC.

There is no available data in the open literature for the viscosity of the CMAS used here at the temperature of the experiments, but one can estimate it from one of the many global statistical glass viscosity

models [40,41]. At 1250 °C the Giordano et al. model [41] gives a viscosity of 11 Pa·s for the present CMAS.

The pressure driving permeation through the inter-columnar pores is driven largely by capillarity, which for flow into a cylindrical conduit is given by [42]:

$$\Delta p = \frac{2\sigma_{LV}}{r} \cos\theta \tag{3}$$

where σ_{LV} is the surface tension of liquid CMAS, r is the inter-columnar pore radius and θ the contact angle. Since the CMAS oxide wets the TBC oxide well, $\cos\theta \rightarrow 1$. The surface tension of these silicate melts has been extensively studied and estimates of $\sim 0.4 \text{ J/m}^2$ have been proposed [23]. Hence, for an inter-columnar pore diameter of $\sim 1 \mu\text{m}$, the estimated pressure driving permeation would be $\sim 1.6 \times 10^6 \text{ Pa}$ ($\sim 16 \text{ atm}$). The capillary pressure in the feathery pores is expected to be much higher due to the much smaller radius, but the permeability is also reduced

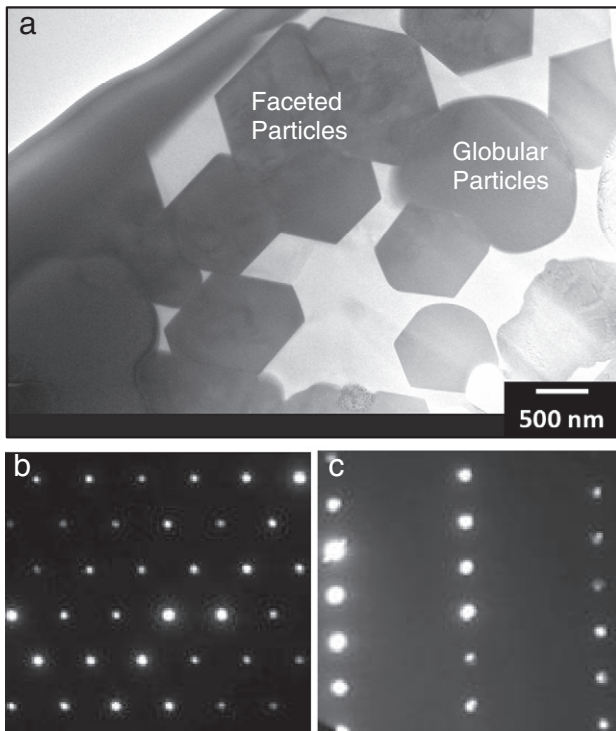


Fig. 13. Bright field TEM images of an area cut by FIB shown in Fig. 12. The SAD patterns of faceted particles in the micrograph correspond to the [001] and [023] zone axis, respectively.

considerably. The results suggest that infiltration of the feathery pores may occur subsequent to that of the intercolumnar gaps.

By integration of Eq. (1), the infiltration time for CMAS to penetrate the coating to a depth L can be estimated from:

$$t = \frac{2\tau^2}{\Gamma \Phi} \left(\frac{\mu}{\sigma_{LV}} \right) L^2. \quad (4)$$

Given an intercolumnar pore fraction $\phi \sim 24\%$ (60% of the total pore volume fraction, based on microscopic measurements), a viscosity $10 \text{ Pa}\cdot\text{s}$, a surface tension $\sigma_{LV} \sim 0.4 \text{ J/m}^2$, the time for molten CMAS to fully penetrate a $200 \mu\text{m}$ thick coating at $1250 \text{ }^\circ\text{C}$ would be $\sim 15 \text{ s}$. The scenario is illustrated schematically in Fig. 14 and is consistent with the observations here as well as in previous studies on conventional EB-PVD coatings, which are somewhat less porous. One may pose the question of whether the dissolution of the TBC can affect the viscosity of the melt and thus its rate of penetration. The current viscosity models do not account for the modifying effect of Y^{3+} and Sm^{3+} incorporated in the CMAS melt. The effect of TBC dissolution on the viscosity is thus not as relevant to the penetration as the potential effect of the dissolved oxides in modifying the crystallization kinetics [28].

In bilayer SZO/YSZ coatings, exposure of SZO to molten CMAS for 1 min at $1250 \text{ }^\circ\text{C}$ resulted in a shallower depth penetration ($\sim 30 \mu\text{m}$) than in 7YSZ as schematically shown in Fig. 14(a). However, after 4 h of CMAS exposure, the entire coating had been completely penetrated and undergone a significant morphological evolution, as schematically depicted in Fig. 14(b). While the reaction formed the expected mixture of fluorite and apatite phases, consistent with the observations on GZO, the penetration was not arrested as in the latter [21]. It has been shown that the time involved in sealing an intercolumnar gap by the dissolution/re-precipitation process depends on the width of the gap [28]. With the substantially higher porosity content of these DVD coatings relative to EB-PVD, and the concomitantly higher probability of wider gaps, it is arguable that the rate of dissolution/re-precipitation

must be significantly higher to seal the higher volume of pores in the SZO coatings here than in those investigated by Krämer et al. [21]. EB-PVD SZO coatings might exhibit reduced penetration, but the only reports in the literature on SZO columnar coatings are those produced by DVD [11].

It is also likely that the dissolution/re-precipitation kinetics of SZO is different from that of GZO, especially if the composition is not uniform. Recent work has shown that the dissolution kinetics of $\text{ZrO}_2\text{-NdO}_{1.5}$ in CMAS depends strongly on the Nd content [43]. Unfortunately, no similar study has been undertaken on SZO, or a comparative study between GZO and SZO. This remains to be elucidated by future investigation.

It is also of interest to consider the situation at the SZO/YSZ interface in the bilayer coatings when CMAS penetrates and concurrently dissolves both oxides. The local dilution of Sm^{3+} in the melt due to the increased concentration of Zr^{4+} from the dissolution of YSZ yields a transition zone where the population of apatite crystals decreases rapidly and that of fluorite increases, the latter with higher proportion of Sm and Ca than of Y (Table 3). The separation of the layers after CMAS attack is believed to occur because of localized dissolution of material at the individual YSZ/SZO interfaces. It is established that CMAS can penetrate the grain boundaries in polycrystalline (plasma sprayed) coatings [44]. However, under proper deposition conditions the YSZ/SZO interface is epitaxial [33], facilitated by the closeness in lattice parameters between t' -YSZ ($a = 0.5111 \text{ nm}$, $c = 0.5169 \text{ nm}$) and the disordered fluorite form of as deposited SZO ($a = 0.5295 \text{ nm}$). The coherency of this interface would suggest a diminished propensity to exhibit local dissolution/penetration by the CMAS melt. It is possible that local stresses due to the CTE mismatch between layers, or the differential sintering of the layers in an isothermal experiment could assist in the dissolution process. There is insufficient information to assess these scenarios but it has been shown that thermal stresses alone are not sufficient to cause delamination in similar bilayer coatings under furnace cycling tests [18]. Nevertheless, it is clearly undesirable for CMAS to penetrate down to this interface, and the interface is needed due to the functionality achieved with the double layer, i.e. low thermal conductivity, top layer phase stability at higher temperatures and CMAS resistance, and improved toughness for the underlayer.

The most remarkable finding of this study was the suppression of CMAS infiltration in a multilayer TBC in which a non-reactive metal (Pt) layer was inserted near the top of the bilayer coating, Fig. 14(b). An approximately $5 \mu\text{m}$ thick, continuous, fully dense platinum layer had been successfully deposited on the inter-columnar structure of the SZO coating and had covered over the inter-columnar gaps [36]. While the Pt dissolution rate in CMAS at $1250 \text{ }^\circ\text{C}$ has not been fully quantified, previous studies in air indicated a very low Pt recession rate (of $\sim 5 \times 10^{-6} \mu\text{m/h}$) at $1100 \text{ }^\circ\text{C}$ [36]. In the situation investigated here the Pt was in contact with CMAS, not air, the temperature was significantly higher, and the rate of Pt loss appeared to be substantially increased. As a consequence, while CMAS permeation was arrested for at least 16 h over most of the coating, its effectiveness as a CMAS barrier layer began to diminish at locally thinner regions of the layer.

We note that the multilayer SZO/Pt/SZO/YSZ coatings are in a compressive stress at the CMAS exposure temperature because all layers have higher coefficients of thermal expansion than the alumina substrate. The compressive stresses eliminate tensile creep fracture of the Pt layer, but the high interfacial free energy per unit area of the Pt/SZO interface provides a driving force for agglomeration of the Pt film. This could lead to hole formation, first in locally thinner regions of the Pt film [45,46]. Once this has occurred, the CMAS melt would then be able to penetrate the platinum layer and begin to enter the ceramic coating via the vertical inter-columnar separations. Because most of the Pt layer remained unbroken at 16 h of CMAS exposure, and thus protective, the CMAS penetration rate through the isolated holes in the platinum layer was low, and the multilayer structure appeared to only gradually (not abruptly) lose its protective function. It is interesting to note that the fully CMAS infiltrated top SZO layer did not delaminate

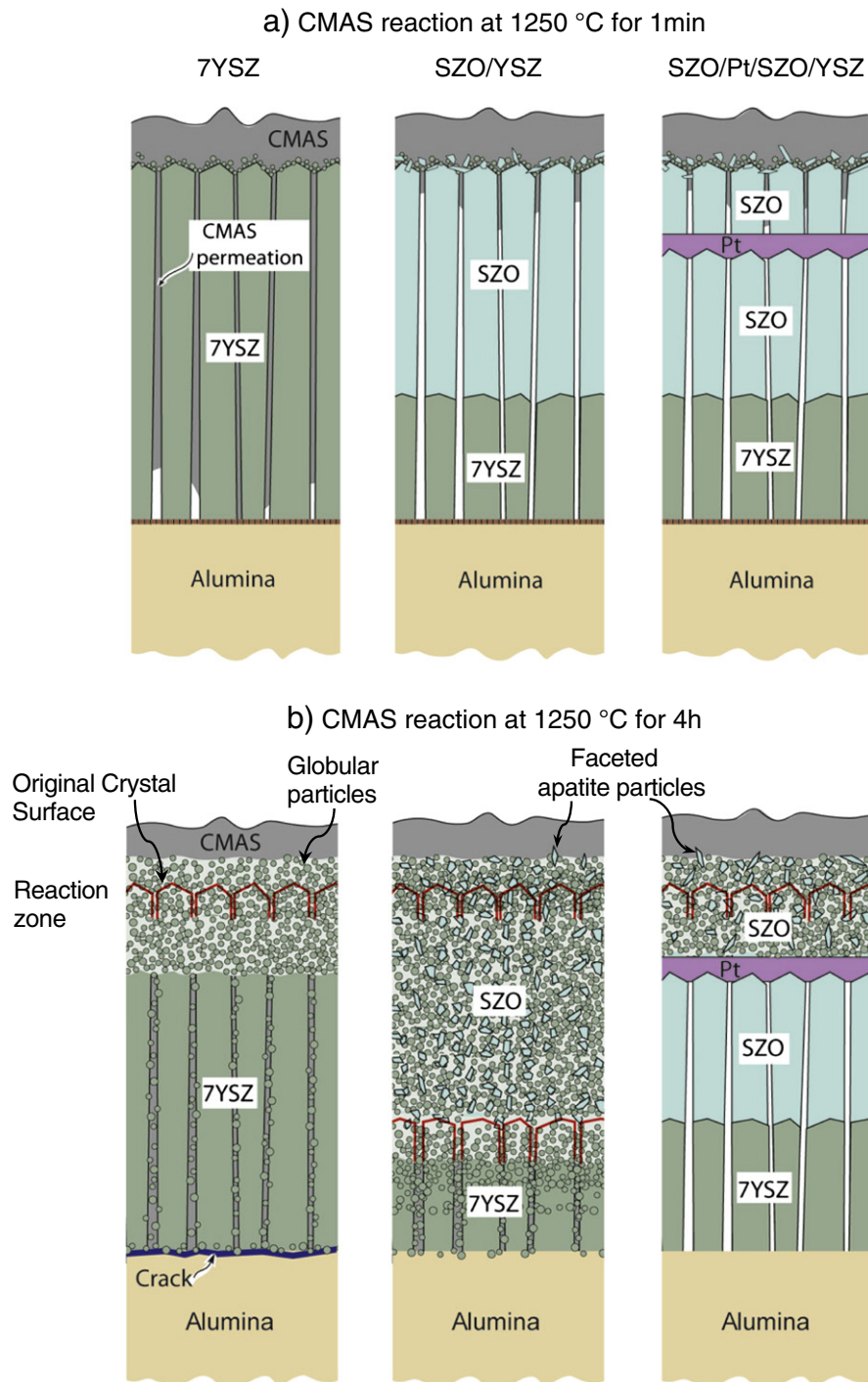


Fig. 14. Stages of CMAS infiltration and reaction in the three types of 200 μm thick thermal barrier coating explored in the study.

from the Pt layer upon cooling. Presumably this was a result of sufficient interfacial toughness at the CMAS–SZO/Pt interface to support the strain energy stored in the (thin) CMAS infiltrated layer. The use of a structure with several Pt layers near the outer surface of the coating might also further impede the progress of CMAS and inhibit delamination.

5. Conclusions

Three different thermal barrier coating systems (7YSZ, SZO on a 7YSZ buffer layer and SZO/Pt/SZO on a 7YSZ buffer layer) have been deposited on alumina substrates using an electron beam directed vapor deposition technique and then exposed to molten CMAS at

1250 °C to investigate their liquid CMAS infiltration response. The mechanisms of CMAS infiltration into the three thermal barrier coating systems have been schematically illustrated in Fig. 14.

The time for CMAS to penetrate a coating is shown to decrease with the intercolumnar pore fraction. Liquid permeability analysis indicated that 200 μm thick DVD 7YSZ coatings would be penetrated by CMAS at 1250 °C in ~ 15 s, which was consistent with the experimental observations. It was found that the higher porosity DVD 7YSZ coatings did not appreciably increase the rate of CMAS penetration over that of conventionally deposited material, which typically contains 50% less porosity.

The rate of CMAS penetration in SZO was slower than that in 7YSZ, but a 100 μm thick SZO/7YSZ bilayer coating was still completely

penetrated after a 4 h exposure. The SZO–CMAS reaction led to formation of both an apatite phase; $[\text{Ca}_{0.59}\text{Sm}_{0.28}\text{□}_{0.13}]_4[\text{Sm}_{0.67}\text{Zr}_{0.33}]_6(\text{SiO}_4)_6\text{O}_2$ and a ZrO_2 -rich solid solution phase with small amounts of Sm and Ca in solid solution. However, the high intercolumn pore volume fraction in the DVD coating reduced the effectiveness of the crystallized reaction products at impeding permeation of the CMAS.

When CMAS penetrated through the SZO layer of a 7YSZ/SZO bilayer coating, reactions between the bilayer coating and CMAS led to SZO/YSZ interface dissolution and separation.

In the SZO/Pt/SZO/YSZ system, CMAS infiltration was arrested by a 5 μm thick Pt layer for about 16 h at 1250 °C, indicating that precious metal layers can disrupt penetration of CMAS in modified TBC coatings. However, over time the Pt was reduced in thickness and small holes began to form through which CMAS started to slowly penetrate. By confining the CMAS infiltrated region to a thin layer at the surface of the coatings, the Pt layers appear to have reduced the strain energy that drives delamination of the infiltrated TBC on cooling. The use of multiple Pt layer near the outer surface of coatings might further ameliorate CMAS infiltration, and the delamination that leads to the eventual loss of coatings in gas turbine engine applications.

Acknowledgments

The authors are grateful to the Office of Naval Research who supported the research (contract # N00014-03-1-0297) under the program direction of Dr. David Shifler. Support for CGL was provided under ONR grant N00014-08-1-0522. The assistance of Dr. James Schiffbauer and Defu Liang with the TEM work is greatly appreciated.

References

- [1] R.A. Miller, *Surf. Coat. Technol.* 30 (1987) 1–11.
- [2] A.G. Evans, D.R. Clarke, C.G. Levi, *J. Eur. Ceram. Soc.* 28 (2008) 1405–1419.
- [3] A.G. Evans, D.R. Mumm, J.W. Hutchinson, G.H. Meier, F.S. Pettit, *Prog. Mater. Sci.* 46 (2001) 505–553.
- [4] S. Stecura, Effects of Compositional Changes on the Performance of a Thermal Barrier Coating System, NASA TM-78976, National Aeronautics and Space Administration, 1978.
- [5] T.E. Strangman, *Thin Solid Films* 127 (1985) 93–106.
- [6] D.D. Hass, H.N.G. Wadley, *J. Vac. Sci. Technol. A Vac. Surf. Films* 27 (2009) 404–414.
- [7] T.J. Lu, C.G. Levi, H.N.G. Wadley, A.G. Evans, *J. Am. Ceram. Soc.* 84 (2001) 2937–2946.
- [8] H. Zhao, Z. Yu, H.N.G. Wadley, *Surf. Coat. Technol.* 204 (2010) 2432–2441.
- [9] H. Lau, C. Leyens, U. Schulz, C. Friedrich, *Surf. Coat. Technol.* 165 (2003) 217–223.
- [10] M.R. Begley, H.N.G. Wadley, *Acta Mater.* 60 (2012) 2497–2508.
- [11] H. Zhao, C.G. Levi, H.N.G. Wadley, *Surf. Coat. Technol.* 203 (2009) 3157–3167.
- [12] J. Wu, X. Wei, N.P. Padture, P.G. Klemens, M. Gell, E. Garcia, P. Miranzo, M.I. Osendi, *J. Am. Ceram. Soc.* 85 (2002) 3031–3035.
- [13] R. Vassen, X. Cao, F. Tietz, D. Basu, D. Stover, *J. Am. Ceram. Soc.* 83 (2000) 2023–2028.
- [14] W. Pan, C.L. Wan, Q. Xu, J.D. Wang, Z.X. Qu, *Thermochim. Acta* 455 (2007) 16–20.
- [15] C.G. Levi, *Curr. Opin. Solid State Mater. Sci.* 8 (2004) 77–91.
- [16] X.Q. Cao, R. Vassen, W. Jungen, S. Schwartz, F. Tietz, D. Stover, *J. Am. Ceram. Soc.* 84 (2001) 2086–2090.
- [17] R. Subramanian, in: Siemens Westinghouse Power Corporation (Orlando, FL), US Patent 6258467, 2001.
- [18] H. Zhao, M.R. Begley, A. Heuer, R. Sharghi-Moshaghini, H.N.G. Wadley, *Surf. Coat. Technol.* 205 (2011) 4355–4365.
- [19] M.P. Borom, C.A. Johnson, L.A. Peluso, *Surf. Coat. Technol.* 86–87 (1996) 116–126.
- [20] A. Aygun, A.L. Vasiliev, N.P. Padture, X. Ma, *Acta Mater.* 55 (2007) 6734–6745.
- [21] S. Krämer, J. Yang, C.G. Levi, *J. Am. Ceram. Soc.* 91 (2008) 576–583.
- [22] T. Strangman, D. Raybould, A. Jameel, W. Baker, *Surf. Coat. Technol.* 202 (2007) 658–664.
- [23] S. Krämer, J. Yang, C.G. Levi, C.A. Johnson, *J. Am. Ceram. Soc.* 89 (2006) 3167–3175.
- [24] X. Chen, *Surf. Coat. Technol.* 200 (2006) 3418–3427.
- [25] C. Mercer, S. Faulhaber, A.G. Evans, R. Darolia, *Acta Mater.* 53 (2005) 1029–1039.
- [26] D.D. Hass, A.J. Slifka, H.N.G. Wadley, *Acta Mater.* 49 (2001) 973–983.
- [27] Y.G. Yang, D.D. Hass, H.N.G. Wadley, *Thin Solid Films* 471 (2005) 1–11.
- [28] C.G. Levi, J.W. Hutchinson, M.-H. Vidal-Sétif, C.A. Johnson, *MRS Bull.* 37 (2012) 932–941.
- [29] M. Freling, D.A. Litton, M.J. Maloney, K.W. Schlichting, J.G. Smeggil, D.B. Snow, in: US7785722 B2, 2010.
- [30] J.E.H. Sansom, D. Richings, P.R. Slater, *Solid State Ionics* 139 (2001) 205–210.
- [31] S.T. Misture, S.P. Harvey, R.T. Franczy, Y.G.S. DeCarr, S.C. Bancheri, *J. Mater. Res.* 19 (2004) 2330–2335.
- [32] J.M. Drexler, A.L. Ortiz, N.P. Padture, *Acta Mater.* 60 (2012) 5437–5447.
- [33] U. Kolitsch, H.J. Scifert, F. Aldinger, *J. Phase Equilib.* 19 (1998) 426–433.
- [34] R.H. Hopkins, N.T. Melamed, T. Henningsen, G.W. Roland, *J. Cryst. Growth* 10 (1971) 218–222.
- [35] M.R. Begley, H.N.G. Wadley, *J. Am. Ceram. Soc.* 94 (2011) s96–s103.
- [36] Z. Yu, H. Zhao, H.N.G. Wadley, *J. Am. Ceram. Soc.* 94 (2011) 2671–2679.
- [37] D.D. Hass, P.A. Parrish, H.N.G. Wadley, *J. Vac. Sci. Technol. A Vac. Surf. Films* 16 (1998) 3396–3401.
- [38] H. Zhao, F. Yu, T.D. Bennett, H.N.G. Wadley, *Acta Mater.* 54 (2006) 5195–5207.
- [39] R.E. Collins, *Flow of Fluids Through Porous Materials*, Reinhold Publishing Co., New York, 1961.
- [40] A. Fluegel, *Glass Technol. Eur. J. Glass Sci. Technol. Part A* 48 (2007) 13–30.
- [41] D. Giordano, J.K. Russell, D.B. Dingwell, *Earth Planet. Sci. Lett.* 271 (2008) 123–134.
- [42] P.-G.d. Gennes, F. Brochard-Wyart, D. Quere, *Capillarity and Wetting Phenomena: Drops, Bubbles, Pearls, Waves*, Springer, 2003.
- [43] N. Chellah, M.-H. Vidal-Setif, C. Petitjean, P.-J. Panteix, C. Rapin, M. Vilasi, 8th International Symposium on High Temperature Corrosion and Protection of Materials (HTCPM8), Les Embiez, France, 2012.
- [44] S. Krämer, S. Faulhaber, M. Chambers, D.R. Clarke, C.G. Levi, J.W. Hutchinson, A.G. Evans, *Mater. Sci. Eng. A* 490 (2008) 26–35.
- [45] D. Srolovitz, M. Goldiner, *JOM* 47 (1995) 31–36.
- [46] S.K. Sharma, J. Spitz, *Thin Solid Films* 65 (1980) 339–350.
- [47] R. Schafrik, Personal Communication (2008).